Magnetic Resonance in Medicine 64:1360–1372 (2010)

Temperature-Induced Tissue Susceptibility Changes Lead to Significant Temperature Errors in PRFS-Based MR Thermometry During Thermal Interventions

Sara M. Sprinkhuizen,[1]* Maurits K. Konings,[2] Martijn J. van der Bom,[1] Max A. Viergever,[1] Chris J. G. Bakker,[1] and Lambertus W. Bartels[1]

Proton resonance frequency shift-based MR thermometry (MRT) is hampered by temporal magnetic field changes. Temporal changes in the magnetic susceptibility distribution lead to nonlocal field changes and are, therefore, a possible source of errors. The magnetic volume susceptibility of tissue is temperature dependent. For water-like tissues, this dependency is in the order of 0.002 ppm/°C. For fat, it is in the same order of magnitude as the temperature dependence of the proton electron screening constant of water (0.01 ppm/°C). For this reason, proton resonance frequency shift-based MR thermometry in fatty tissues, like the human breast, is expected to be prone to errors. We aimed to quantify the influence of the temperature dependence of the susceptibility on proton resonance frequency shift-based MR thermometry. Heating experiments were performed in a controlled phantom set-up to show the impact of temperature-induced susceptibility changes on actual proton resonance frequency shift-based temperature maps. To study the implications for a clinical case, simulations were performed in a 3D breast model. Temperature errors were quantified by computation of magnetic field changes in the glandular tissue, resulting from susceptibility changes in a thermally heated region. The results of the experiments and simulations showed that the temperature-induced susceptibility changes of water and fat lead to significant errors in proton resonance frequency shift-based MR thermometry. Magn Reson Med 64:1360–1372, 2010. ©2010 Wiley-Liss, Inc.

Key words: susceptibility; temperature; PRFS-based MR thermometry; HIFU; fat; glandular tissue

Next to excellent soft-tissue contrast, MRI also offers methods to acquire temperature maps, which allow for monitoring and guiding of thermal interventions. Proton resonance frequency shift (PRFS)-based MR thermometry (MRT) is the most commonly used temperature monitoring technique. It is based on the temperature dependence of the proton resonance frequency (PRF) of protons in water molecules and is thus applicable in water-containing tissues. The technique does not work for protons in fat molecules and for this reason adequate fat suppression is essential for accurate thermometry in tissues containing both water and fat.

PRFS-based MRT is hampered by temporal field changes. In the application of this technique, the contribution of field changes, which originate from temperature-induced magnetic volume susceptibility changes, is commonly ignored. This disregards the fact that the magnetic volume susceptibility χ (which will hereinafter be referred to as "susceptibility") of water and water-containing tissue is temperature dependent (1,2). Several studies have suggested that this may lead to PRFS-based temperature errors in water and water-containing tissues (1–4). This has been shown for water (3) and brain tissue (2), which both have a temperature dependent susceptibility in the order of $d\chi/dT = 0.002$ ppm/°C.

In tissues containing both water and fat, more considerable susceptibility-related problems may occur. For fat tissue, the temperature dependence of the susceptibility has been reported to be $d\chi_{fat}/dT = 0.0094$ ppm/°C (1) and $d\chi_{fat}/dT = 0.00804$ ppm/°C (2). Changes in the susceptibility distribution lead to magnetic field changes, which occur not only locally at the site of the susceptibility change, but also arise nonlocally in the surroundings of the susceptibility change. Consequently, in tissues containing both water and fat, e.g., the human breast, the PRF in the water-containing glandular tissue is also affected by temperature-induced susceptibility changes in the surrounding fat tissue. This may hamper PRFS-based temperature measurements in composite tissues. To date, no attention has been paid to the quantification of this effect, in spite of the fact that it may be significant and that its influence on PRFS-based MRT is not eliminated by fat-suppression techniques.

In this study, we aimed to quantify the influence of the temperature dependence of the susceptibility of water and fat on PRFS-based MR temperature maps, both experimentally and theoretically. First, controlled water-fat phantom heating experiments were conducted to demonstrate the occurrence of temperature-induced susceptibility-related temperature errors in actual PRFS-based MR temperature maps. To study the implications for a clinical case, simulations were performed to predict the errors in PRFS-based measurements during a thermal therapy procedure in human tissue. For this we used a model of the female breast, as thermal ablation of breast tumors is an emerging minimally invasive therapeutic intervention. Breast tumors originate in glandular tissue and are mostly surrounded by fat. Susceptibility-related temperature errors are, therefore, expected to occur when

[1]Image Sciences Institute/Department of Radiology, University Medical Center Utrecht, Utrecht, The Netherlands.

[2]Department of Medical Technology, University Medical Center Utrecht, Utrecht, The Netherlands.

Grant sponsor: STW UGT-6771.

*Correspondence to: Sara M. Sprinkhuizen, M.Sc., Image Sciences Institute/Department of Radiology, University Medical Center Utrecht, Utrecht, The Netherlands. E-mail: sara@isi.uu.nl

Received 10 February 2010; revised 14 April 2010; accepted 18 May 2010.

DOI 10.1002/mrm.22531

Published online 20 July 2010 in Wiley Online Library (wileyonlinelibrary.com).

PRFS-based MRT is used to monitor a thermal procedure in the breast. Temperature errors in the glandular tissue were quantified by computation of the magnetic field changes, resulting from temperature-induced susceptibility changes in a thermally heated region. As the magnitude of the temperature errors is determined by the susceptibility distribution, which is related to the shape of the anatomy of interest as well as the shape of the heating pattern, various orientations and sizes of the heated region were analyzed, to study the impact on the temperature errors.

THEORY

The susceptibility distribution inside and outside an arbitrarily shaped object depends on the temperature distribution $T(\mathbf{r})$. From a certain susceptibility distribution $\chi(\mathbf{r},T(\mathbf{r}))$ that is placed in a uniform external magnetic field B_0, the macroscopic magnetic field B_{mac} can be derived from Maxwell's equations in matter. The PRF at a certain location inside an object is proportional to the magnetic field experienced by the hydrogen nuclei at that location, B_{nuc}. This local magnetic field B_{nuc} is a result of screening of the nuclei from the macroscopic magnetic field in the object, B_{mac}, by microscopic current distributions, described by the proton electron screening constant $\sigma(\mathbf{r},T(\mathbf{r}))$ and the susceptibility of the object $\chi(\mathbf{r},T(\mathbf{r}))$, which are both temperature dependent (1):

$$B_{nuc}(\mathbf{r},T(\mathbf{r})) = \left(1-\sigma(\mathbf{r},T(\mathbf{r}))-\frac{2}{3}\chi(\mathbf{r},T(\mathbf{r}))\right)B_{mac}(\chi(\mathbf{r},T(\mathbf{r}))) \quad [1]$$

The macroscopic magnetic field may be approximated by $B_{mac} = B_0 + O(\chi B_0)$ in case of nonmagnetic or weakly magnetic materials like human tissues ($|\chi| < 1$), which leads to:

$$B_{nuc}(\mathbf{r},T(\mathbf{r})) \cong B_{mac}(\chi(\mathbf{r},T(\mathbf{r}))) - \left(\sigma(\mathbf{r},T(\mathbf{r}))+\frac{2}{3}\chi(\mathbf{r},T(\mathbf{r}))\right)B_0 \quad [2]$$

In PRFS-based MRT, temperature-induced field changes in B_{nuc} are extracted from the phase difference $\Delta\varphi$ between successive gradient echo MR images, acquired at temperatures T and T_{ref}, respectively:

$$\Delta\varphi = \varphi-\varphi_{ref} = -\gamma TE(B_{nuc}(\mathbf{r},T(\mathbf{r}))-B_{nuc}(\mathbf{r},T_{ref}(\mathbf{r}))) = -\gamma TE\left(\Delta B_{mac}-\left(\Delta\sigma+\frac{2}{3}\Delta\chi\right)B_0\right) \quad [3]$$

with γ the gyromagnetic ratio, TE the echo time, $\Delta B_{mac} = B_{mac}(\chi(\mathbf{r},T(\mathbf{r}))) - B_{mac}(\chi_{ref}(\mathbf{r},T_{ref}(\mathbf{r})))$ and $\Delta\sigma$ and $\Delta\chi$ being the temperature-induced changes in the proton electron screening constant and susceptibility, respectively. Note the minus sign that indicates clockwise rotation in a right-handed Cartesian coordinate system. The temperature change, which is measured with PRFS-based MRT, ΔT_{PRFS}, is computed from the phase difference, using:

$$\Delta T_{PRFS} = \frac{\Delta\varphi}{\alpha\gamma B_0 TE} \quad [4]$$

Here, it is commonly assumed that the only temperature dependency that needs to be taken into account in the proportionality constant α is that of the proton electron screening constant of water, σ_{water}, with $\alpha = d\sigma_{water}/dT = 0.01$ ppm/°C (5). In literature on PRFS-based MRT, this definition for α is not strictly used and negative values for α occur. In some papers, the σ in Eq. 1 is erroneously referred to as the chemical shift, and α is thus referred to as the temperature dependence of the chemical shift. This is regardless of the fact that the chemical shift, δ, is defined as $\delta[\text{ppm}] = (\sigma_{ref}-\sigma)\cdot 10^6$, with σ_{ref} the screening constant of a reference molecule. To put it accurately: with increasing temperature, the electron screening of water increases, and the chemical shift decreases (thus $d\delta_{water}/dT = -0.01$ ppm/°C). Here, the strict derivation for α based on the electron screening constant is used. In the ideal situation, in which the assumption regarding σ_{water} as the only temperature dependent parameter holds, the temperature change is given by:

$$\Delta T_{ideal} = \frac{\Delta\sigma}{\alpha} \quad [5]$$

However, as shown in Eq. 3, reality differs from the ideal situation in the sense that the temperature dependence of the susceptibility distribution also plays a role. When the actually measured phase change (Eq. 3) is substituted in Eq. 4, this yields:

$$\Delta T_{PRFS} = -\frac{1}{\alpha}\left(\frac{\Delta B_{mac}}{B_0}-\Delta\sigma-\frac{2}{3}\Delta\chi\right) \quad [6]$$

The difference between the measured temperature change ΔT_{PRFS} and the ideal temperature change ΔT_{ideal} gives the temperature error ε_T:

$$\varepsilon_T = -\frac{1}{\alpha}\left(\frac{\Delta B_{mac}}{B_0\Delta T}-\frac{2}{3}\frac{\Delta\chi}{\Delta T}\right) \quad [7]$$

Equation 7 shows that the temperature error ε_T is subject to changes in B_{mac} and χ. The macroscopic field in itself also depends on changes in the susceptibility distribution, which means that temperature errors are induced by local (χ) and nonlocal (B_{mac}) susceptibility changes.

The contributions of temperature-induced susceptibility changes to the PRF are usually ignored in PRFS-based MRT. This is a problematic approach, for two reasons. First, by neglecting the local susceptibility changes of the water-containing tissue, temperature errors occur (3), even though the temperature dependence of the susceptibility of water is small: $d\chi_{water}/dT = 0.00199$ ppm/°C (2). Second, changes in $\chi(\mathbf{r},T(\mathbf{r}))$ alter the macroscopic field B_{mac}, which affects the PRF, and hence the measured temperature, of all water protons that experience

this field change. Temperature measurements in water-containing tissue may, therefore, be corrupted by nonlocal field effects due to susceptibility changes in the surroundings of the tissue. This raises a realistic problem in tissues where fat is present, e.g., breast tissue, because the temperature dependence of the susceptibility of fat, χ_{fat}, is reported to be in the same order of magnitude as the temperature dependence of the proton electron screening constant of water ($d\chi_{fat}/dT = 0.0094$ ppm/°C (1) and $d\chi_{fat}/dT = 0.00804$ ppm/°C (2)). Consequently, temperature-induced susceptibility changes of fat in the surroundings of a tumor may affect the magnetic field experienced by the water protons within the tumor.

METHODS

Heating Experiments

To demonstrate the impact of temperature-induced susceptibility changes on actual PRFS-based MR temperature maps, controlled phantom heating experiments were conducted. The phantom consisted of a large circular container (Ø = 28 cm, height = 8 cm), filled with deionized water, in which a Perspex cylinder (outer radius = 22 mm; inner radius = 20 mm; length = 77 mm) was placed, such that the long axis of the cylinder was aligned perpendicular to the main magnetic field. This cylinder contained the fluid of interest, of which the temperature, and, hence, susceptibility was altered during the experiment. Two different fluids were examined: in the first experiment, the cylinder was filled with the same deionized water as was used in the outer container. In the second experiment, the cylinder was filled with sunflower oil. Sunflower oil was chosen because it conveniently allowed for fast exchange between scans, as will be described below. At the start of both experiments, the temperature of the water in the outer container was equal to the temperature of the fluid within the cylinder (≈21°C). For both set-ups, 70 dynamic coronal single slice PRFS-based MRT scans were acquired through the center of the cylinder. The first 10 PRFS-based MRT scans were acquired with the whole phantom at constant temperature. The fluid inside the fixed cylinder was quickly replaced in between scans 10 and 11 with identical, but heated, fluid (accomplished by placing the fluid in a warm water bath with a constant temperature of 75°C for 1 h before scanning) using a large syringe.

The magnitude of the temperature errors is determined by the susceptibility and temperature distribution. The phantom set-up was designed such that the temperature errors in the PRFS-based temperature maps were expected to appear as a dipole field pattern surrounding the cylinder. This is shown by the following equation, which gives the microscopic field change (ΔB_{nuc}) caused by susceptibility changes, outside an infinite cylinder (perpendicular to B_0), in a plane perpendicular to the long axis:

$$\Delta B_{nuc} = \frac{\Delta\chi_e}{3} B_0 + \frac{\Delta\chi_e - \Delta\chi_i}{2} R^2 \frac{(x^2 - z^2)}{(x^2 + z^2)^2} B_0 \qquad [8]$$

with R the radius of the cylinder and $\Delta\chi_e$ and $\Delta\chi_i$ the susceptibility changes outside and inside the cylinder, respectively. This equation shows that, for a coronal PRFS-based temperature map and $\Delta\chi_e = 0$, a positive $\Delta\chi_i$ leads to positive field offsets in the direction of z (B_0), and to negative field offsets over the x-axis. This corresponds to a temperature underestimation over the z-axis and a temperature overestimation over the x-axis. To validate the true temperature during all scans at these two locations, two optical temperature fibers were positioned at ~1.5 mm from the edge of the cylinder. The PRFS-based temperature was averaged within a region of interest (2 × 2 voxels) at these two locations for all scans. The temporal behavior of the PRFS-based temperature changes in the water surrounding the cylinder was then compared to the temperature as measured with the optical fibers. A third optical fiber was placed inside the cylinder to monitor the temperature of the heated fluid over the whole duration of the experiment.

All scans were performed on a 1.5-T whole body MRI scanner (Achieva, Philips Healthcare, Best, The Netherlands), and the following scan parameters were used for a single slice spoiled gradient echo scan: FOV 300 × 300 mm^2; acquired voxel size: 1.875 × 1.875 × 4 mm^3; flip angle $\alpha = 30°$; number of signal averages = 1; read-out gradient G_R = 11 mT/m; TE = 15 msec and TR = 50 msec. Dynamic scan time = 8 sec. Total scan time (70 dynamics) = 9 min and 21 sec.

Simulation Technique

In PRFS-based MRT, the susceptibility-related field changes are erroneously interpreted as a temperature-change. Discrimination between susceptibility-related field changes and other (e.g., proton electron screening related) effects is not feasible during a thermal procedure in vivo. Therefore, simulations were performed to calculate the susceptibility related field changes. To quantify the influence of susceptibility changes on PRFS-based MRT, the corresponding, χ-related, magnetic field changes in B_{nuc} need to be determined:

$$\Delta B_{nuc}(\chi) = \left(\frac{\Delta B_{mac}}{B_0 \Delta T} - \frac{2}{3} \frac{\Delta\chi}{\Delta T} \right) \qquad [9]$$

It has been indicated by several authors that the use of the Fourier transform to calculate magnetic field changes from a given susceptibility distribution is advantageous (6,7). It is possible to derive a relation between the magnetizing field H and the susceptibility distribution χ using the Fourier-based approach (6). However, as the B field is a direct observable related to the Larmor frequency, whereas the H-field is not a direct observable, we have chosen to use the relation between the susceptibility distribution $\chi(\boldsymbol{r},T(\boldsymbol{r}))$ and the observable B field itself. The derivation is shown in Appendix I.

The input for each simulation consisted of two susceptibility distributions, $\chi(\boldsymbol{r},T_{ref}(\boldsymbol{r}))$ and $\chi(\boldsymbol{r},T_{incr}(\boldsymbol{r}))$, where $T_{ref}(\boldsymbol{r})$ is the preheating, starting temperature distribution and $T_{incr}(\boldsymbol{r})$ is the postheating, increased temperature distribution. Using the Fourier-based technique, the microscopic field B_{nuc} was then computed for both the preheating and postheating susceptibility distribution. The corresponding field change ΔB_{nuc} was found by

subtraction of the preheating from the postheating outcome, and expressed in ppm using: $\Delta B_{\text{nuc}}[\text{ppm}] = \frac{\Delta B_{\text{nuc}}[\text{Tesla}]}{B_0[\text{Tesla}]} \cdot 10^6$. Subsequently, the temperature error was computed, using Eq. 7. The negative proportionality of $\Delta B_{\text{nuc}}(\chi)$ and ε_T is apparent: negative $\Delta B_{\text{nuc}}(\chi)$ values lead to a temperature overestimation, and positive $\Delta B_{\text{nuc}}(\chi)$ values lead to a temperature underestimation. We aim to quantify the errors in temperature measurements that are related to susceptibility changes and it is therefore that in our simulations, ΔB_{nuc} exclusively incorporates temperature-related susceptibility effects, and no proton electron screening effects.

For numerical accuracy, the computational volume was taken at least a factor of two larger than the object of interest for all simulations. The matrix size was 256 × 256 × 256 for all computations.

Simulation of Phantom Experiments

The results from the phantom heating experiment were compared to the outcome of the Fourier-based simulation technique. The expected temperature errors around the cylinder were calculated based on a 3D model of the cylindrical phantom, in which the following susceptibility values were used for the fluid inside the cylinder:

$$\chi_{\text{water}}(T) = -9.05 \cdot 10^{-6} + 0.002 \cdot 10^{-6} \cdot \Delta T \qquad [10]$$

$$\chi_{\text{oil}}(T) = -8.53 \cdot 10^{-6} + 0.0055 \cdot 10^{-6} \cdot \Delta T \qquad [11]$$

based on χ_{water} as reported in (8), $d\chi_{\text{water}}/dT$ from (9), and with ΔT the temperature change of the fluid. The volume susceptibility of sunflower oil was calculated based on the density (0.919 g/cm^3 (10)) and the molar susceptibility and molar mass of the constituent fatty acids (10,11) [mole% fatty acid (molar susceptibility (10^{-3} cm^3/mol), molar mass (g/mol))]: 7% palmitic (−2.50, 256.42); 63% linoleic (−2.51, 280.45); 25% oleic (−2.62, 282.46); 5% stearic (−2.77, 284.48). The temperature dependence of the susceptibility of the oil was computed using a volume thermal expansion coefficient of $0.654 \cdot 10^3$ (12): $d\chi_{\text{oil}}/dT = 0.0055$ ppm/°C. The susceptibility of Perspex is reported to be: $\chi_{\text{Perspex}} = -9 \times 10^{-6}$ (13). The temperature dependence of χ_{Perspex} was computed from the linear thermal expansion coefficient (0.7 mm/m/10°C) and the density of the Perspex (1.2 g/cm^3), yielding: $d\chi_{\text{Perspex}}/dT = -0.0019$ ppm/°C, which is the same as water. For this reason, the Perspex layer was not separately modeled but instead was assigned the same susceptibility properties as the surrounding water.

The temperature error around the cylinder was computed for a range of temperatures of the fluid inside the cylinder. The optically measured temperature of the fluid during the experiment was used to correlate the PRFS-based temperature to the simulated temperature error. The susceptibility of the water surrounding the cylinder was kept constant in the simulations.

Susceptibility-Related Temperature Error Quantification in the Female Breast

To study the implications of the temperature dependence of the susceptibility on MRT measurements in a realistic setting, simulations were performed. MR-guided High Intensity Focused Ultrasound (MRgHIFU) in the breast was chosen as a model for the quantification of susceptibility-induced MR temperature errors. MRgHIFU ablation is a therapeutic modality of which the potential for the noninvasive treatment of benign and malignant breast tumors has been shown (14–22). A 3D breast model was used, based on an anatomical data set of a breast tumor patient. A high resolution T1w 3D breast MRI scan of a 63-year-old female breast cancer (invasive ductal carcinoma) patient was used, to obtain spatial distributions of water and fat in a realistic geometry. Written informed consent was obtained from the patient. The tumor (0.7 × 0.7 × 0.7 cm^3) was located at 4.8 cm from the mamilla in the upper outer quadrant of the left breast. The glandular tissue and tumor tissue of the left breast were semiautomatically segmented using a region growing procedure. Smoothing was applied using a gaussian kernel ($\sigma = 1$, kernel size = 7). Outside the segmented glandular and tumor tissues, it was assumed that only fat was present.

To simulate the effect of a thermal intervention using HIFU, a thermal spot was placed in the breast model at the location of the tumor. A typical shape of the thermal focus of a focused ultrasound transducer is an ellipsoid. Multiple thermal spot sizes were modeled. The thermal spot diameter was varied from 1 mm to 8 mm, in steps of 1 mm. The length/diameter ratio was kept 2.5 for all simulated thermal spots. The largest thermal spot had a diameter of 8 mm and a length of 20 mm. During thermal ablation procedures in the breast, a maximum temperature increase of $\Delta T = 49.9$°C has been reported (20). For our simulations, we used a more conservative value of $\Delta T = 30$°C. In all ellipsoidal thermal spots, a stationary gaussian temperature distribution was modeled ($\sigma = 4$, kernel size = ½ · thermal spot diameter) with a maximum temperature of 67°C ($T_{\text{ref}} = 37$°C, $\Delta T = 30$°C).

Not only the size of the thermal spot but also the position of the HIFU transducer with regard to the patient affects the shape of the heating pattern, and thus the distribution of ΔB_{nuc}, within the patient. In most reports on MR-guided HIFU of the breast, the transducer was sonicating parallel to the anteroposterior axis. In one report, the transducer was sonicating parallel to the coronal plane (19). Therefore, all simulations were performed at three different orthogonal orientations of the thermal spot with respect to the main magnetic field.

The following volume susceptibility values were retrieved from the literature, and used for the simulations in the breast model:

$$\chi_{\text{glandular}}(T) = -9.05 \cdot 10^{-6} + 0.002 \cdot 10^{-6} \cdot \Delta T \qquad [12]$$

$$\chi_{\text{fat}}(T) = -7.79 \cdot 10^{-6} + 0.0094 \cdot 10^{-6} \cdot \Delta T \qquad [13]$$

using χ_{fat} as reported in (11) and $d\chi_{\text{fat}}/dT$ from (1). The susceptibility of the tumor tissue was taken to be equal to that of the glandular tissue. For both the preheating breast model (without a thermal spot) and all thermal therapy models, the 3D susceptibility distribution was calculated per voxel, using a weighted average of the local glandular tissue/fat tissue-fraction (Wiedemann's law) and the local temperature. Subsequently, the ΔB_{nuc}

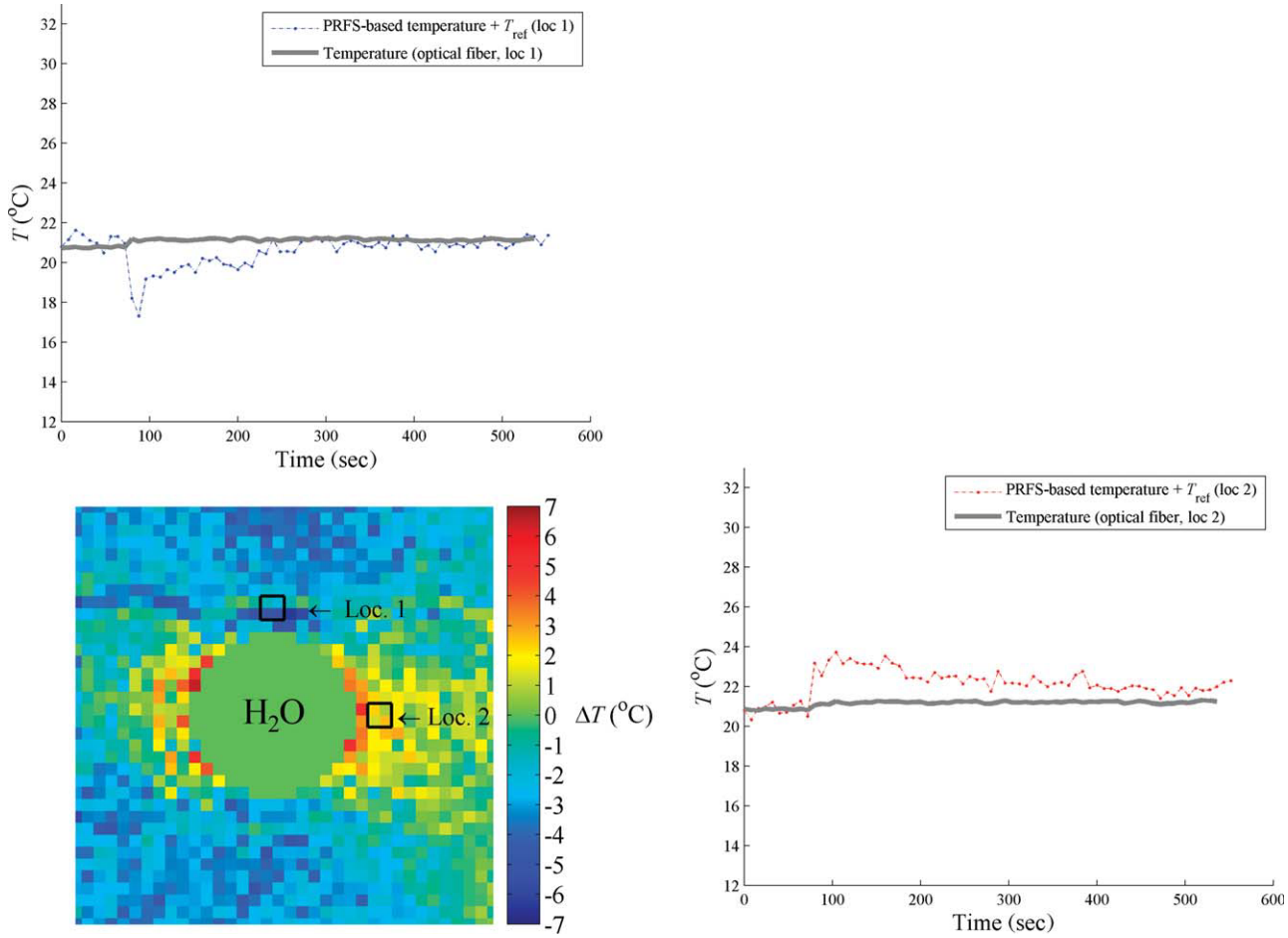

FIG. 1. The PRFS-based temperature map of scan number 12 of the water heating experiment is (partially) shown at the bottom left. In the temperature map, the two regions from which the average temperature over time was taken are indicated by black boxes. At these two locations, optical fiber temperature measurements were acquired. Per location, the optical temperature is compared to the PRFS-based temperature in the graphs above and to the right of the temperature map. [Color figure can be viewed in the online issue, which is available at wileyonlinelibrary.com.]

field was calculated and converted to a 3D temperature error map. The temperature errors at the location of the tumor are of particular interest, as they will affect the thermal dose calculations at the tumor site. To quantify the range of temperature errors within the tumor, the following steps were taken: first, the tumor was manually segmented. Then, all voxels from the 3D temperature error map that were located within this tumor region were visualized in a histogram (one per thermal spot orientation) for all thermal spot sizes.

RESULTS

Heating Experiments

Figures 1 and 2 display the results of the heating experiments of water and oil, respectively. To visually emphasize the nonlocal influence of changes in χ, the temperature values inside the cylinder were not shown. In Fig. 1, the results of the experiment with temperature changes in water are displayed. The PRFS-based temperature map of scan number 12 is shown (bottom left). This is the second scan after administration of the heated water, as scan 11 suffered from minor flow-artifacts in the outer container due to the movement of the MR table after administration of the heated fluid. In this temperature map, a dipole-field pattern can be appreciated around the cylinder: the PRFS-based temperature is decreased over the *z*-axis of the cylinder, and increased over the *x*-axis.

At the top left and bottom right, the PRFS-based temperature profiles over time at two locations around the cylinder are plotted (dashed lines) together with the optical fiber data (bold lines). Note that the starting temperature (as measured with the optical fibers) was added to the PRFS temperature profiles (which measure only temperature changes). The dipole-behavior is clearly apparent: after administration of the heated water, the measured PRFS-based temperature change at location 1 decreased ($\Delta T = -2.9$°C), whereas at location 2, it increased ($\Delta T = +2.3$°C). The true temperature, measured with the optical fiber, showed only a slight temperature increase at both locations, of +0.4°C maximum.

For the heating experiment in sunflower oil, shown in Fig. 2, this behavior was also observed. The PRFS-based temperature map of scan number 12 (bottom left) shows a more pronounced dipole field pattern around the cylinder, as was expected based on the stronger temperature

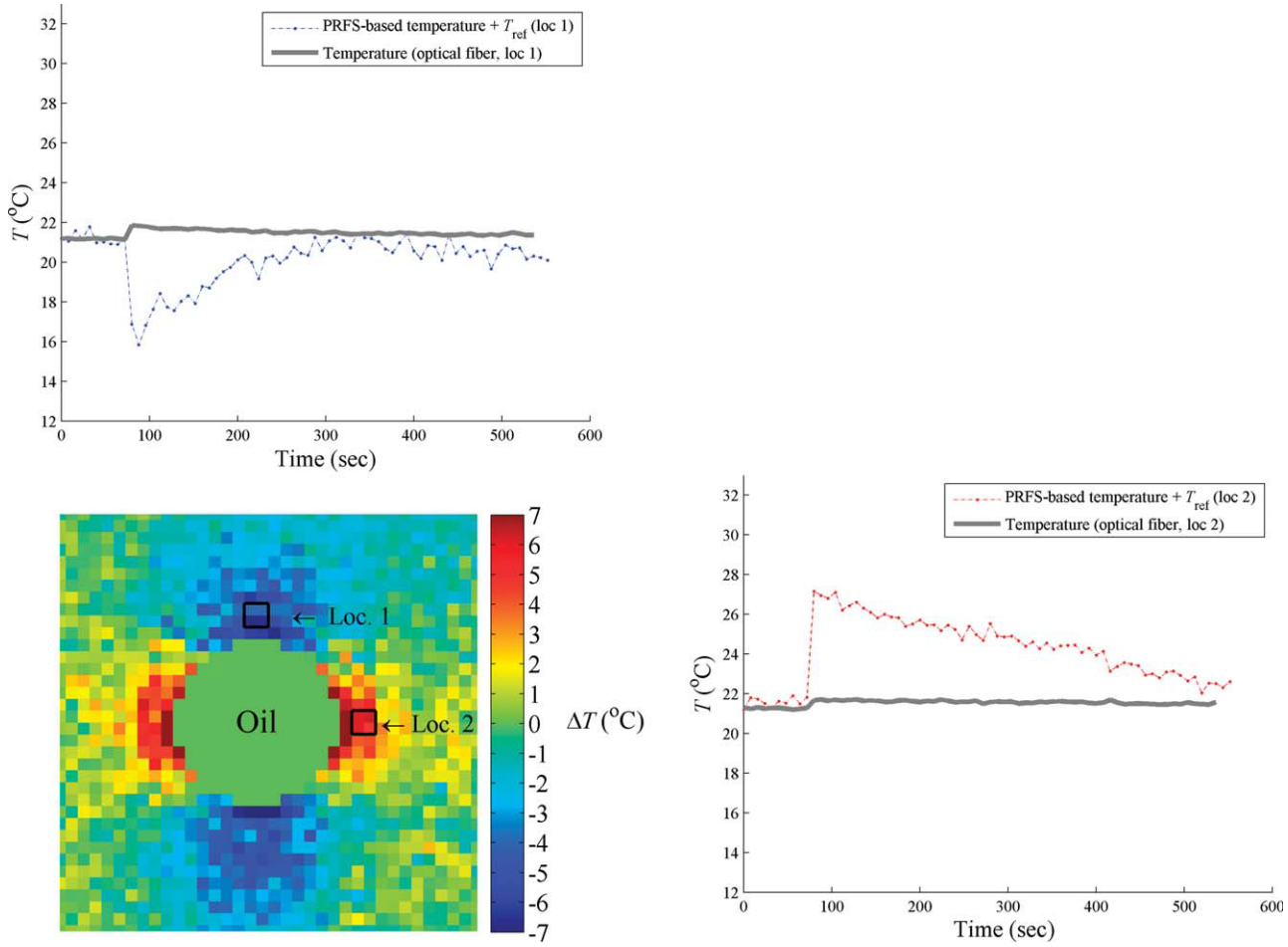

FIG. 2. The PRFS-based temperature map of scan number 12 of the oil heating experiment is (partially) shown at the bottom left. In the temperature map, the two regions from which the average temperature over time was taken are indicated by black boxes. At these two locations, optical fiber temperature measurements were acquired. Per location, the optical temperature is compared to the PRFS-based temperature in the graphs above and to the right of the temperature map. [Color figure can be viewed in the online issue, which is available at wileyonlinelibrary.com.]

dependence of χ_{fat} compared to χ_{water}. The PRFS-based temperature profiles over time (dashed lines) were compared with the true optical measured temperature (bold lines) at two locations (top left and bottom right). At location 1, the measured PRFS-based temperature decreased between scan 10 and 11 ($\Delta T = -4.3°C$), whereas at location 2, the PRFS-based temperature increased ($\Delta T = +5.6°C$). Again, the true temperature only moderately increased at both locations (+0.7°C maximum).

Simulation of Phantom Experiments

In Fig. 3, the outcome of the simulations is compared to the results for the water (left) and oil (right) heating experiment. The top row shows the PRFS-based MR temperature maps of scan number 12. The middle row shows the two corresponding simulated temperature error maps. The simulations are based on the susceptibility changes within the cylinder, which were calculated using Eq. 10, Eq. 11 and the true temperature of the fluid inside the cylinder, which was measured with the optical fiber ($\Delta T = 40.9°C$ for the water experiment, and $\Delta T = 47.5°C$ for the oil experiment).

The bottom row compares the experimental temperature error with the simulated error over time. The experimental temperature error was calculated by subtraction of the PRFS-based temperature from the optical fiber temperature, per location. The simulated temperature error was found by averaging the calculated ε_T values within a region of interest that corresponds to the region that was used in the experimental analysis (depicted as the black/gray boxes in the simulated error map). The simulated results correlate well with the experimental findings for water. In case of the heated oil experiment, the simulated temperature error is overall larger at location 1 and slightly smaller at location 2. Generally, the temporal behavior of the measured temperature error corresponds to the simulated error.

Susceptibility-Related Temperature Error Quantification in the Female Breast

Figure 4a shows a single slice of the anatomical T1w 3D breast MRI scan in which fat tissue is bright and glandular tissue is dark. Figure 4b shows sections of three orthogonal slices taken from the 3D breast model that was

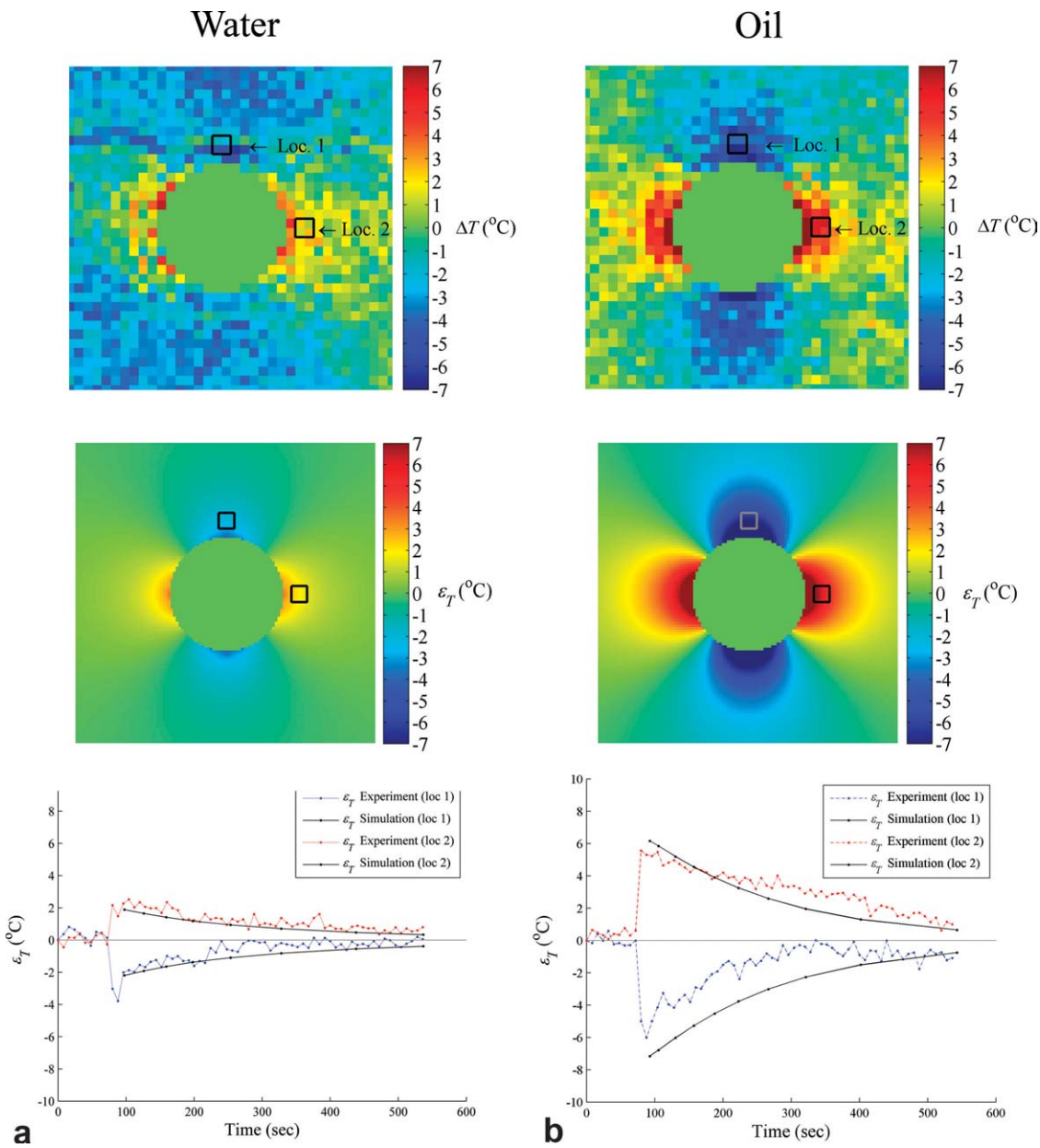

FIG. 3. Experimentally measured temperature change (top row) and simulated temperature error (middle row) are shown for the heating experiment with water (**a**) and oil (**b**). The bottom row shows the experimental and simulated temperature error over time. The experimental temperature error is determined by subtracting the optical temperature from the PRFS-based temperature which was averaged within a region (black boxes). The simulated temperature error is computed by averaging the simulated values in a region at the same two locations as were used experimentally (black/gray boxes).

computed from the anatomical dataset. In these segmented images, the glandular tissue is depicted bright, and fat tissue is shown in black. The tumor tissue was manually segmented in 3D for the quantification of ε_T within the tumor and is visualized in this figure by a red overlay.

The top rows of Figs. 5–7 show the temperature distribution (color-scaled) as induced by a thermal spot with a diameter of 8 mm (length = 20 mm), with relation to the glandular tissue (in white), for all three orientations of the thermal spot (*z*-axis, *x*-axis, and *y*-axis, respectively). Per figure, sections of three orthogonal slices through the breast model are displayed. The bottom rows of Figs. 5–7 show the corresponding temperature error maps. These maps show the distribution of ε_T in and around the tumor. The figures show that the ε_T pattern is related to the orientation of the thermal spot. The maximum temperature error found in glandular tissue in the whole breast model ranged between: −8.6°C and +2.6°C (thermal spot along *z*-axis); −4.9°C and +6.0°C (thermal spot along *x*-axis); −4.0°C and +6.2°C (thermal spot along *y*-axis).

Figure 8 shows the histograms of the ε_T distribution within the tumor, for all sizes of the thermal spot

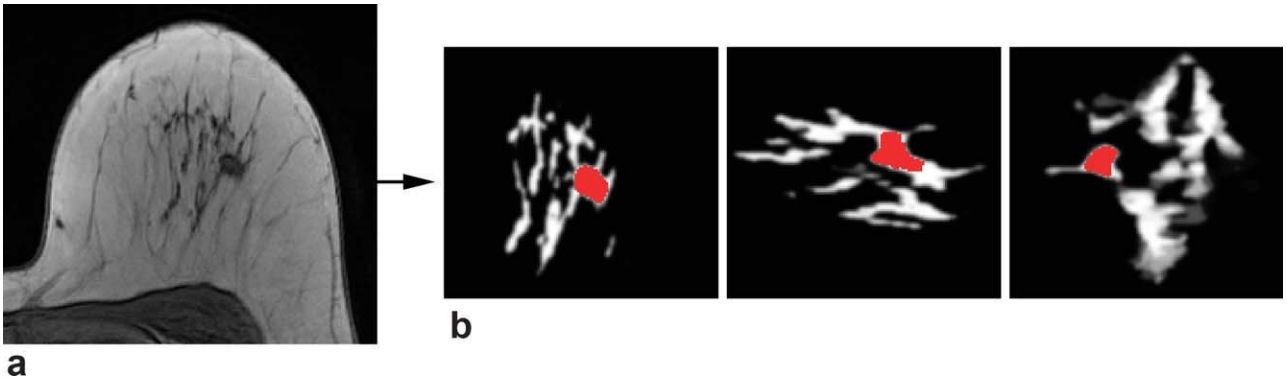

FIG. 4. **a**: A single slice of the anatomical T1w 3D breast MRI scan, in which fat tissue (bright) and glandular tissue (dark) is discernible. From the anatomical dataset, a 3D breast model is computed, containing the distribution of glandular and fat tissue in 3D. **b**: (parts of) Three orthogonal slices through this breast model, the glandular tissue is depicted bright and fat tissue is shown in black. The tumor tissue is segmented for quantification purposes and shown in red. [Color figure can be viewed in the online issue, which is available at wileyonlinelibrary.com.]

(indicated by the thermal spot diameter). From the histograms, an evident relation between the orientation of the thermal spot and the temperature error ε_T inside the tumor can be observed. The orientation of thermal spot in the z direction led to a temperature underestimation of about 4–6°C, whereas the orientation of the thermal spot in the x or y direction led to an overestimation of 2–3°C. Furthermore, all three histograms show that the spread in temperature errors increased with the size of the thermal spot, i.e., susceptibility-related temperature errors increased when more fat was heated.

DISCUSSION AND CONCLUSIONS

We have shown both experimentally and theoretically that temperature-induced susceptibility changes can lead to changes in the magnetic field, which can introduce significant temperature errors in PRFS-based MRT. The experimental results provided proof for the fact that susceptibility changes affect the PRFS-based MRT method nonlocally. This was shown in a phantom set-up where water and oil were locally heated. The PRFS-based temperature around the heated region showed large deviations when compared to optical fiber measurements. The PRFS-

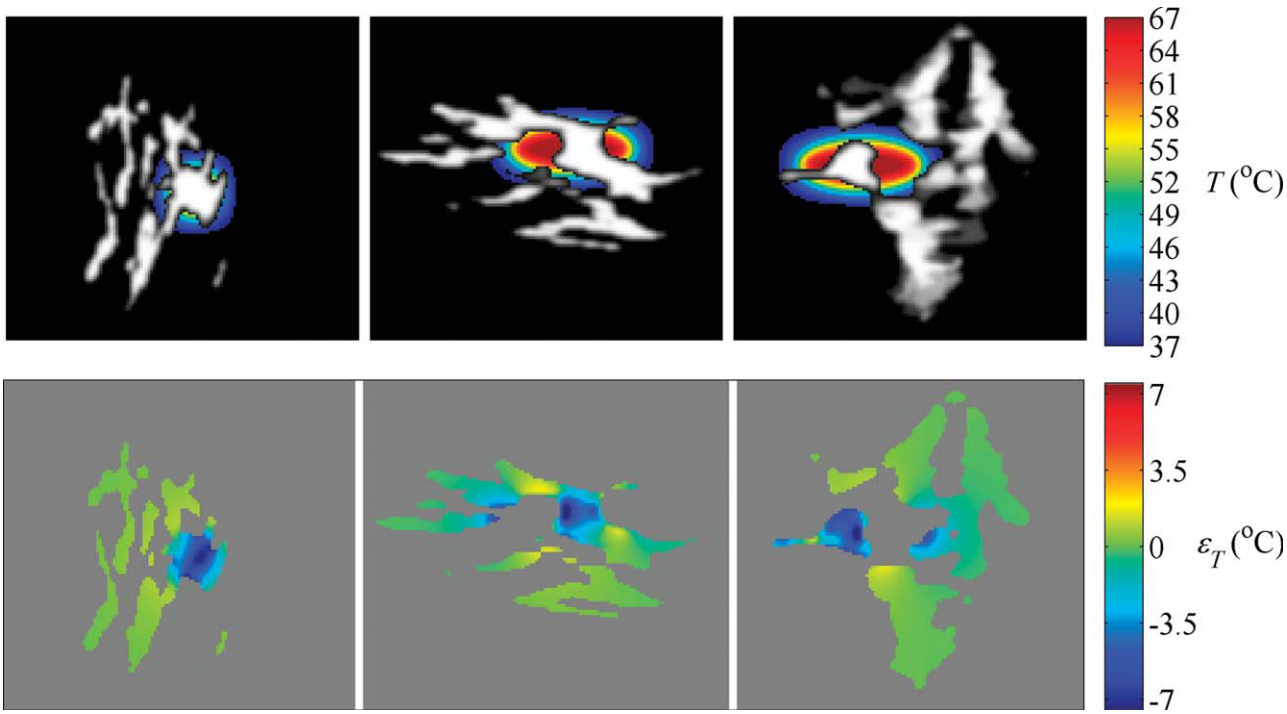

FIG. 5. This figure shows three orthogonal (sections of) slices through the temperature distribution as induced by a thermal spot which is oriented along the z-axis (diameter = 8 mm; length = 20 mm) with relation to the glandular tissue (top row). The corresponding temperature error ε_T maps are also given (bottom row). The maximum temperature errors found in the glandular tissue ranged between −8.6°C and +2.6°C. [Color figure can be viewed in the online issue, which is available at wileyonlinelibrary.com.]

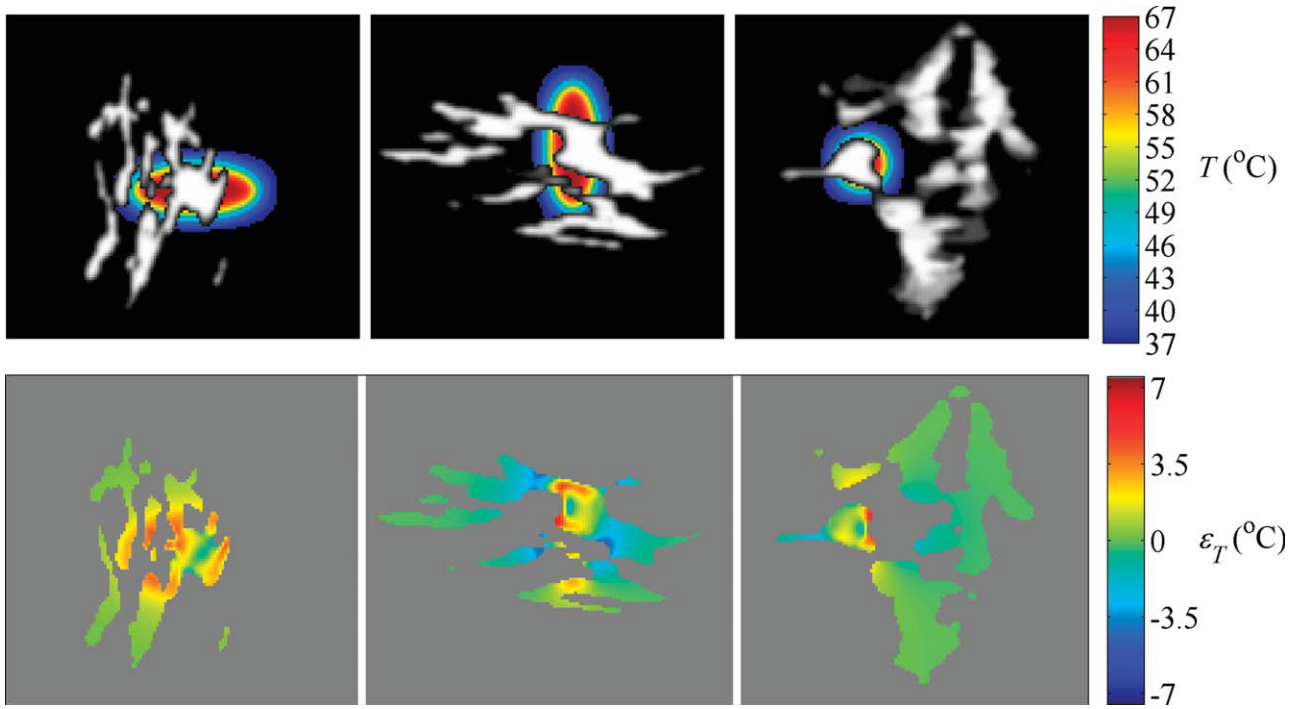

FIG. 6. This figure shows three orthogonal (sections of) slices through the temperature distribution as induced by a thermal spot which is oriented along the *x*-axis (diameter = 8 mm; length = 20 mm) with relation to the glandular tissue (top row). The corresponding temperature error ε_T maps are also given (bottom row). The maximum temperature errors found in the glandular tissue ranged between −4.9°C and +6.0°C. [Color figure can be viewed in the online issue, which is available at wileyonlinelibrary.com.]

based measured temperature changes around the cylinder containing the heated fluid ranged between −2.9°C and +2.3°C for water, and between −4.3°C and +5.6°C for oil, where the optical temperature showed only a slight temperature increase of +0.7°C maximum. The employed simulation technique supported the experimental findings.

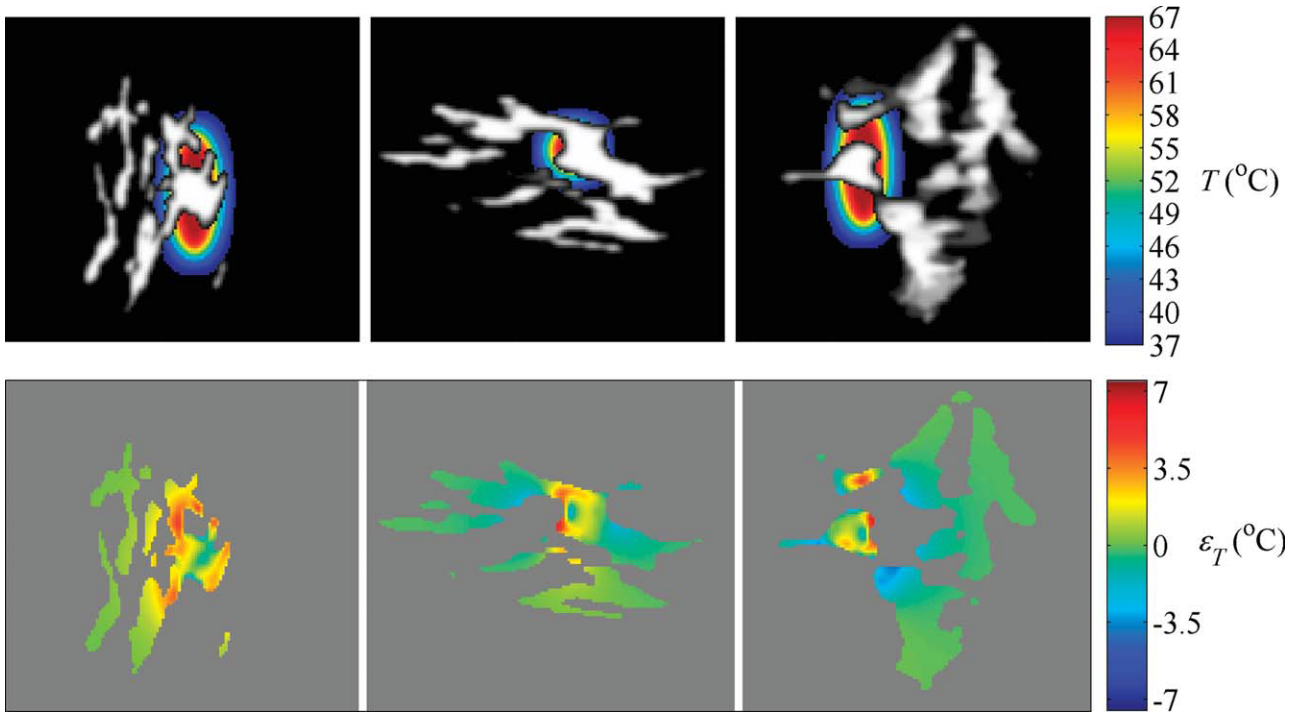

FIG. 7. This figure shows three orthogonal (sections of) slices through the temperature distribution as induced by a thermal spot which is oriented along the *y*-axis (diameter = 8 mm; length = 20 mm) with relation to the glandular tissue (top row). The corresponding temperature error ε_T maps are also given (bottom row). The maximum temperature errors found in the glandular tissue ranged between −4.0°C and +6.2°C. [Color figure can be viewed in the online issue, which is available at wileyonlinelibrary.com.]

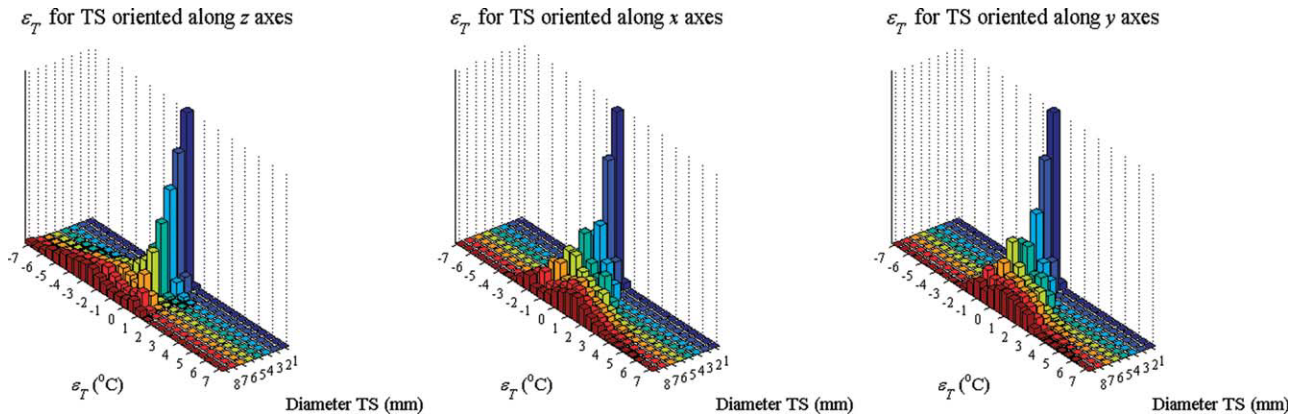

FIG. 8. Three histograms of the temperature error ε_T within the tumor, each corresponding to an orientation of the thermal spot. Per histogram, ε_T is given for all sizes of the thermal spot applied (expressed in diameter). The histograms clearly show an increase of temperature error in the tumor with increasing thermal spot size. Also, a remarkable correlation with the thermal spot orientation and ε_T is shown. For a thermal spot oriented along the *z*-axis (left histogram), an underestimation of the temperature is seen, whereas a thermal spot which is oriented along the *x*- or *y*-axis (middle and right histograms) leads to a temperature overestimation. [Color figure can be viewed in the online issue, which is available at wileyonlinelibrary.com.]

Simulations were performed to quantify the susceptibility-related temperature errors in a breast tumor during thermal ablation using HIFU. Breast tumors are situated in the glandular tissue and are surrounded by fat. During HIFU ablation in the breast, a margin of at least 10 mm around the tumor is necessary to ensure thermal coagulation of the whole lesion (17), which inevitably leads to heating of fat in the surroundings of the tumor. Real-time thermometry can be used to automatically steer the HIFU energy deposition during MRgHIFU therapy using a closed feedback control loop and a volumetric heating strategy (23). To warrant the safety of this approach, the acquisition of reliable MR temperature maps is a prerequisite (15,17). The thermal dose, which can be computed from the temperature evolution over time (24), is also an important characteristic for the guidance of thermal therapy, since it is a noninvasive measure for tissue necrosis, and can thus determine the thermal treatment effectiveness and duration. Over a certain period, for temperatures above 43°C, a temperature increase of 1°C doubles the thermal dose. As a consequence, temperature errors of that order may have a major impact on the treatment guidance. Our simulations showed that for the chosen anatomy, an ellipsoidal HIFU thermal spot of diameter 8 mm and length 20 mm and a maximum temperature increase of $\Delta T = 30$°C led to temperature errors in the glandular tissue ranging between −8.6°C and +6.2°C, depending orientation of the focal spot. The errors within the tumor were of particular interest and ranged between −6°C and +3°C. Errors of this order of magnitude may significantly influence the accuracy of thermal dose calculations during thermal therapy.

The largest diameter of the tumor in this study was about 0.7 cm in all three dimensions. For larger tumors, under certain heating conditions, there may be less susceptibility-related temperature errors in the center of the tumor than for smaller tumors. However, total coagulation is important also at the tumor boundaries, where susceptibility-related errors will occur if the tumor is adjacent to heated fat tissue, regardless of the tumor size.

The shape and size of the heated area were shown to be of influence. An ellipsoidal thermal spot that was aligned with the *z*-axis led to temperature underestimations within the tumor, whereas when it was aligned with the *x*- or *y*-axis, it mainly led to a temperature overestimation at that location. This is due to the fact that changing the orientation and shape of the heating pattern (covering a heterogeneous mixture of aqueous and fatty tissue) influences the susceptibility distribution and thereby the temperature errors in the local temperature inside and outside the thermal spot measured with PRFS-based MRT. The most frequently used breast HIFU systems currently use a transducer that sonicates parallel to the *y*-axis so that temperatures at the tumor location are overestimated. Nevertheless, transducers that sonicate parallel to the coronal (the *x*-*z*) plane are also utilized. In that case, the temperature error is very much dependent on the angle of sonication within that plane.

We investigated temperature-induced changes in the susceptibility. However, temperature is not the only mechanism leading to a change in tissue susceptibility. For example, the susceptibility may change due to alterations in the balance of oxygenated and deoxygenated hemoglobin and myoglobin (2,4). Also, changes in tissue shape and size (e.g., caused by edema) are of possible influence. The incorporation of susceptibility related effects in the computation of PRFS-based temperature maps is not straightforward, due to the unconfined characteristic of the phenomenon.

The influence of susceptibility on PRFS-based MRT is currently mostly ignored. We have shown that temperature errors do occur. This may induce erroneous thermal dose calculations which may have an important influence on the outcome of the thermal treatment. This effect is not eliminated when fat suppression techniques are used. Susceptibility-related temperature errors are not only related to the shape and orientation of the heating pattern but also depend on the distribution of water and fat inside the heated area. The compensation of susceptibility-related temperature errors is, therefore, not

straightforward and requires in-depth analysis of each specific case.

APPENDIX

The following section describes the Fourier-based simulation technique as is used in this article. The magnetic field distribution, which arises from a known susceptibility distribution $\chi(\mathbf{r})$ placed in a homogeneous external magnetic field, is computed, starting with the general equation:

$$\nabla \times \mathbf{B} = \mu_0(\mathbf{J}_{\mathbf{free}} + \nabla \times \mathbf{M}) \quad [A1]$$

in which $\mathbf{M}$ is the magnetization vector of the tissue. Inside the bore of the MRI scanner, there are no primary current sources, and hence $\mathbf{J}_{\mathbf{free}} = \mathbf{0}$ inside the bore. As a result, we have:

$$\nabla \times \mathbf{B} = \mu_0 \nabla \times \mathbf{M} \quad [A2]$$

Furthermore, the rotation of $\mathbf{M}$ may be replaced by an equivalent current density distribution $\mathbf{J}_{\mathbf{equiv}}$:

$$\nabla \times \mathbf{M} = \mathbf{J}_{\mathbf{equiv}} \quad [A3]$$

Therefore, to calculate $\mathbf{B}$, the equivalent current density field $\mathbf{J}_{\mathbf{equiv}}$ is required. By definition, we have

$$\mathbf{M} = \chi \mathbf{H} \quad [A4]$$

Combining Eq. A4 with the general vector equality $\nabla \times (p\mathbf{Q}) = -\mathbf{Q} \times (\nabla p) + p(\nabla \times \mathbf{Q})$ for any scalar p and vector $\mathbf{Q}$, yields:

$$\nabla \times \mathbf{M} = \nabla \times (\chi \mathbf{H}) = -\mathbf{H} \times (\nabla \chi) + \chi(\nabla \times \mathbf{H}) \quad [A5]$$

As $\nabla \times \mathbf{H} = \mathbf{J}_{\mathbf{free}} = \mathbf{0}$ inside the bore, this reduces to

$$\nabla \times \mathbf{M} = \nabla \times (\chi \mathbf{H}) = -\mathbf{H} \times (\nabla \chi) \quad [A6]$$

and hence, using Eq. A3 we have

$$\mathbf{J}_{\mathbf{equiv}} = -\mathbf{H} \times (\nabla \chi) \quad [A7]$$

In MRI, it is customary to work with the magnetic field $\mathbf{B}$ rather than the auxiliary vector $\mathbf{H}$. As by definition $\mathbf{H} = \frac{1}{\mu}\mathbf{B}$, Eq. 8 becomes:

$$\mathbf{J}_{\mathbf{equiv}} = -\frac{1}{\mu}\mathbf{B} \times (\nabla \chi) \quad [A8]$$

in which the recursive nature becomes apparent: the presence of a non-zero $\mathbf{J}_{\mathbf{equiv}}$ at one point in space affects the $\mathbf{B}$ field (and hence $\mathbf{J}_{\mathbf{equiv}}$) at another point in space. In the application at hand, however, the values of χ are small (for biological tissues, χ values are typically of the order of magnitude of 10^{-6}), and hence replacing $\frac{1}{\mu}\mathbf{B}$ by $\frac{1}{\mu_0}\mathbf{B}_0$ in Eq. A8 results in only a small relative error of order $O(\chi)$ in the calculation of $\mathbf{J}_{\mathbf{equiv}}$:

$$\mathbf{J}_{\mathbf{equiv}} = -\frac{1}{\mu_0}\mathbf{B}_0 \times (\nabla \chi)(1 + O(\chi)) \quad [A9]$$

At this point, we neglect the error of order $O(\chi)$, and calculate $\mathbf{J}_{\mathbf{equiv}}$ directly from the known $\mathbf{B}_0$ and the given susceptibility distribution χ using:

$$\mathbf{J}_{\mathbf{equiv}} = -\frac{1}{\mu_0}\mathbf{B}_0 \times (\nabla \chi) \quad [A10]$$

Using these equivalent currents as a substitute for materials with magnetic susceptibility, the $\mathbf{B}$-field is now completely determined by only free currents and equivalent currents in a vacuum ($\mu = \mu_0$ everywhere):

$$\nabla \times \mathbf{B} = \mu_0(\mathbf{J}_{\mathbf{free}} + \mathbf{J}_{\mathbf{equiv}}) \quad [A11]$$

For any superposition of current density distributions, the resulting $\mathbf{B}$-field is the sum of the $\mathbf{B}$-fields from each separate current density distribution. In the case of Eq. A11, $\mathbf{J}_{\mathbf{free}} = \mathbf{0}$ inside the bore; we are only interested in the $\mathbf{B}$-field arising from $\mathbf{J}_{\mathbf{equiv}}$. Let the $\mathbf{B}$-field arising from $\mathbf{J}_{\mathbf{equiv}}$ be denoted as $\delta\mathbf{B}$. Once the $\mathbf{J}_{\mathbf{equiv}}$ distribution has been calculated using Eq. A10, the $\delta\mathbf{B}$ field can be calculated using a vector potential, as is explained below. In analogy to the general equation $\nabla^2\mathbf{A} = -\mu_0\mathbf{J}$, we define $\mathbf{A}_{\mathbf{equiv}}$ as the vector potential that arises from the $\mathbf{J}_{\mathbf{equiv}}$ distribution:

$$\nabla^2 \mathbf{A}_{\mathbf{equiv}} = -\mu_0 \mathbf{J}_{\mathbf{equiv}} \quad [A12]$$

To calculate the $\mathbf{A}_{\mathbf{equiv}}$ from Eq. A12, we use a Fourier technique, as will be explained in more detail further below. First, however, to indicate how the $\delta\mathbf{B}$ field follows from the $\mathbf{A}_{\mathbf{equiv}}$ field once the $\mathbf{A}_{\mathbf{equiv}}$ field is calculated, we combine the general vector equality $\nabla^2\mathbf{Q} = -\nabla(\nabla \cdot \mathbf{Q}) - \nabla \times (\nabla \times \mathbf{Q})$ (for any vector $\mathbf{Q}$) with $\nabla \cdot \mathbf{A}_{\mathbf{equiv}} = \mathbf{0}$ (because the magnetic field is stationary) to obtain:

$$\nabla^2 \mathbf{A}_{\mathbf{equiv}} = -\nabla \times (\nabla \times \mathbf{A}_{\mathbf{equiv}}) \quad [A13]$$

In combination with Eq. A12 and $\nabla \times \delta\mathbf{B} = \mu_0\mathbf{J}_{\mathbf{equiv}}$ (Eq. A11) this leads to

$$\delta\mathbf{B} = \nabla \times \mathbf{A}_{\mathbf{equiv}} \quad [A14]$$

We now focus on calculating $\mathbf{A}_{\mathbf{equiv}}$ from the $\mathbf{J}_{\mathbf{equiv}}$ distribution. Solving Eq. A12 yields:

$$\mathbf{A}_{\mathbf{equiv}}(\mathbf{r}) = \frac{\mu_0}{4\pi}\int d^3\xi \frac{\mathbf{J}_{\mathbf{equiv}}(\boldsymbol{\xi})}{|\mathbf{r} - \boldsymbol{\xi}|} \quad [A15]$$

In Eq. A15, the advantages of performing the calculations in the Fourier-domain are apparent because of the convolution operator inside the equation. The equation can be written symbolically as

$$\begin{aligned} A_x &= \frac{\mu_0}{4\pi} J_x * G \\ A_y &= \frac{\mu_0}{4\pi} J_y * G \\ A_z &= \frac{\mu_0}{4\pi} J_z * G \end{aligned} \quad [A16]$$

in which

$$\mathbf{J_{equiv}} = (J_x, J_y, J_z) \quad [A17]$$

$$\mathbf{A_{equiv}} = (A_x, A_y, A_z) \quad [A18]$$

$$G(\mathbf{r} - \boldsymbol{\xi}) = \frac{1}{|\mathbf{r} - \boldsymbol{\xi}|} \quad [A19]$$

Let the following lowercase symbols $\mathbf{a_{equiv}}(\mathbf{k})$, $\delta\mathbf{b}(\mathbf{k})$, $\mathbf{j_{equiv}}(\mathbf{k})$, $\theta(\mathbf{k})$ denote the Fourier transforms of $\mathbf{A_{equiv}}(\mathbf{r})$, $\delta\mathbf{B}(\mathbf{r})$, $\mathbf{J_{equiv}}(\mathbf{r})$, and $\chi(\mathbf{r})$, respectively. Using the integral:

$$\frac{1}{|\mathbf{r} - \boldsymbol{\xi}|} = \frac{1}{\pi}\int \mathrm{d}^3k \frac{e^{-i2\pi\mathbf{k}\cdot(\mathbf{r}-\xi)}}{k^2} \quad [A20]$$

we have

$$g(\mathbf{k}) = \frac{1}{\pi k^2} \quad [A21]$$

Furthermore, since the Fourier transform of $\nabla\chi(\mathbf{r})$ equals $-i2\pi\mathbf{k}\theta(\mathbf{k})$, and since $\mathbf{J_{equiv}}(\mathbf{r}) = -(1/\mu_0)\ \mathbf{B}_0 \times \nabla\chi(\mathbf{r})$, and $\mathbf{B}_0$ is a constant vector field pointing along the z-axis ($\mathbf{B}_0 = B_0\hat{\mathbf{z}}$), we have:

$$\mathbf{j_{equiv}}(\mathbf{k}) = \frac{2\pi B_0}{\mu_0}\begin{pmatrix} ik_y\theta(\mathbf{k}) \\ -ik_x\theta(\mathbf{k}) \\ 0 \end{pmatrix} \quad [A22]$$

and

$$\mathbf{a_{equiv}}(\mathbf{k}) = \frac{1}{2\pi}B_0\begin{pmatrix} ik_y\theta(\mathbf{k})/k^2 \\ -ik_x\theta(\mathbf{k})/k^2 \\ 0 \end{pmatrix} \quad [A23]$$

Furthermore, the Fourier transform of $\delta\mathbf{B} = \nabla\times\mathbf{A_{equiv}}$ (see above) yields $\delta\mathbf{b} = -2\pi i\mathbf{k} \times \mathbf{a_{equiv}}$. Therefore, we now have::

$$\delta\mathbf{b}(\mathbf{k}) = B_0\begin{pmatrix} k_xk_z\theta(k)/k^2 \\ k_yk_x\theta(k)/k^2 \\ -(k_x^2 + k_y^2)\theta(\mathbf{k})/k^2 \end{pmatrix} \quad [A24]$$

As a result, the desired $\delta\mathbf{B}(\mathbf{r})$ field can now be found by calculating the inverse Fourier transform of $\delta\mathbf{b}(\mathbf{k})$, which on its turn is calculated from the given $\theta(\mathbf{k})$ using Eq. A24:

$$\chi(\mathbf{r}) \xrightarrow{F} \theta(\mathbf{k}) \overset{\text{Eq.A24}}{\rightarrow} \delta\mathbf{b}(\mathbf{k}) \xrightarrow{F^{-1}} \delta\mathbf{B}(\mathbf{r}) \quad [A25]$$

Note that this calculated $\delta\mathbf{B}(\mathbf{r})$ field is the deviation from the $\mathbf{B}_0$ field and is given in Tesla. The component of $\delta\mathbf{B}(\mathbf{r})$ along the z-direction is taken. The macroscopic magnetic field is then given by: $B_{\mathrm{mac}} = B_0 + \delta B$. The last step is the computation of the total microscopic field B_{nuc}. For our purpose, the changes in the B_{nuc} field that are related to temperature-induced susceptibility changes in the object are of importance. Therefore, in this case, the electron screening constant term can be excluded from Eq. 1:

$$B_{\mathrm{nuc}}(\mathbf{r}, T(\mathbf{r})) = \left(1 - \frac{2}{3}\chi(\mathbf{r}, T(\mathbf{r}))\right)B_{\mathrm{mac}}(\chi(\mathbf{r}, T(\mathbf{r}))) \quad [A26]$$

REFERENCES

1. De Poorter J. Noninvasive MRI thermometry with the proton resonance frequency method: study of susceptibility effects. Magn Reson Med 1995;34:359–367.
2. Stollberger R, Ascher PW, Huber D, Renhart W, Radner H, Ebner F. Temperature monitoring of interstitial thermal tissue coagulation using MR phase images 2. J Magn Reson Imaging 1998;8: 188–196.
3. Peters RD, Hinks RS, Henkelman RM. Heat-source orientation and geometry dependence in proton-resonance frequency shift magnetic resonance thermometry. Magn Reson Med 1999;41: 909–918.
4. Young IR, Hajnal JV, Roberts IG, Ling JX, Hill-Cottingham RJ, Oatridge A, Wilson JA. An evaluation of the effects of susceptibility changes on the water chemical shift method of temperature measurement in human peripheral muscle. Magn Reson Med 1996;36: 366–374.
5. Hindman JC. Proton resonance shift of water in the gas and liquid states. J Chem Phys 1966;44:4582–4592.
6. Salomir R, Denis de Senneville B, Moonen CT. A fast calculation method for magnetic field inhomogeneity due to an arbitrary distribution of bulk susceptibility. Concepts Magn Reson B: Magn Reson Eng 2003;19B:26–34.
7. Marques JP, Bowtell R. Application of a Fourier-based method for rapid calculation of field inhomogeneity due to spatial variation of magnetic susceptibility. Concepts Magn Reson B 2005;25B:65–78.
8. Schenck JF. The role of magnetic susceptibility in magnetic resonance imaging: MRI magnetic compatibility of the first and second kinds. Med Phys 1996;23:815–850.
9. Philo JS, Fairbank WM. Temperature dependence of the diamagnetism of water. J Chem Phys 1980;72:4429.
10. Lide DR, editor. CRC Handbook of Chemistry and Physics, 90th ed. (Internet Version 2010), Boca Raton, FL: CRC Press/Taylor and Francis.
11. Hopkins JA, Wehrli FW. Magnetic susceptibility measurement of insoluble solids by NMR: magnetic susceptibility of bone. Magn Reson Med 1997;37:494–500.
12. Coupland JN, McClements JD. Physical properties of liquid edible oils J Am Oil Chem Soc 1997;74:1559–1564.
13. Moerland MA, Beersma R, Bhagwandien R, Wijrdeman HK, Bakker CJ. Analysis and correction of geometric distortions in 1.5 T magnetic resonance images for use in radiotherapy treatment planning. Phys Med Biol 1995;40:1651–1654.
14. Furusawa H, Namba K, Nakahara H, Tanaka C, Yasuda Y, Hirabara E, Imahariyama M, Komaki K. The evolving non-surgical ablation of breast cancer: MR guided focused ultrasound (MRgFUS). Breast Cancer 2007;14:55–58.
15. Furusawa H, Namba K, Thomsen S, Akiyama F, Bendet A, Tanaka C, Yasuda Y, Nakahara H. Magnetic resonance-guided focused ultrasound surgery of breast cancer: reliability and effectiveness. J Am Coll Surg 2006;203:54–63.
16. Gianfelice D, Khiat A, Amara M, Belblidia A, Boulanger Y. MR imaging-guided focused ultrasound surgery of breast cancer: correlation of dynamic contrast-enhanced MRI with histopathologic findings. Breast Cancer Res Treat 2003;82:93–101.
17. Gianfelice D, Khiat A, Amara M, Belblidia A, Boulanger Y. MR imaging-guided focused US ablation of breast cancer: histopathologic assessment of effectiveness—initial experience. Radiology 2003;227: 849–855.
18. Gianfelice D, Khiat A, Boulanger Y, Amara M, Belblidia A. Feasibility of magnetic resonance imaging-guided focused ultrasound surgery as an adjunct to tamoxifen therapy in high-risk surgical patients with breast carcinoma. J Vasc Interv Radiol 2003;14:1275–1282.
19. Huber PE, Jenne JW, Rastert R, Simiantonakis I, Sinn HP, Strittmatter HJ, von Fournier D, Wannenmacher MF, Debus J. A new noninvasive

approach in breast cancer therapy using magnetic resonance imaging-guided focused ultrasound surgery. Cancer Res 2001;61:8441–8447.
20. Hynynen K, Pomeroy O, Smith DN, Huber PE, McDannold NJ, Kettenbach J, Baum J, Singer S, Jolesz FA. MR imaging-guided focused ultrasound surgery of fibroadenomas in the breast: a feasibility study. Radiology 2001;219:176–185.
21. Khiat A, Gianfelice D, Amara M, Boulanger Y. Influence of post-treatment delay on the evaluation of the response to focused ultrasound surgery of breast cancer by dynamic contrast enhanced MRI. Br J Radiol 2006;79:308–314.
22. Zippel DB, Papa MZ. The use of MR imaging guided focused ultrasound in breast cancer patients; a preliminary phase one study and review. Breast Cancer 2005;12:32–38.
23. Mougenot C, Quesson B, de Senneville BD, de Oliveira PL, Sprinkhuizen S, Palussiere J, Grenier N, Moonen CT. Three-dimensional spatial and temporal temperature control with MRT-guided focused ultrasound (MRgHIFU). Magn Reson Med 2009;61: 603–614.
24. Sapareto SA, Dewey WC. Thermal dose determination in cancer therapy. Int J Radiat Oncol Biol Phys 1984;10:787–800.